IEEE Photonics Journal
An IEEE Photonics Society Publication

Volumetric Method of Moments and Conceptual Multilevel Building Blocks for Nanotopologies

Volume 4, Number 1, February 2012

X. Zheng
V. K. Valev
N. Verellen
Y. Jeyaram
A. V. Silhanek
V. Metlushko
M. Ameloot
G. A. E. Vandenbosch, Senior Member, IEEE
V. V. Moshchalkov

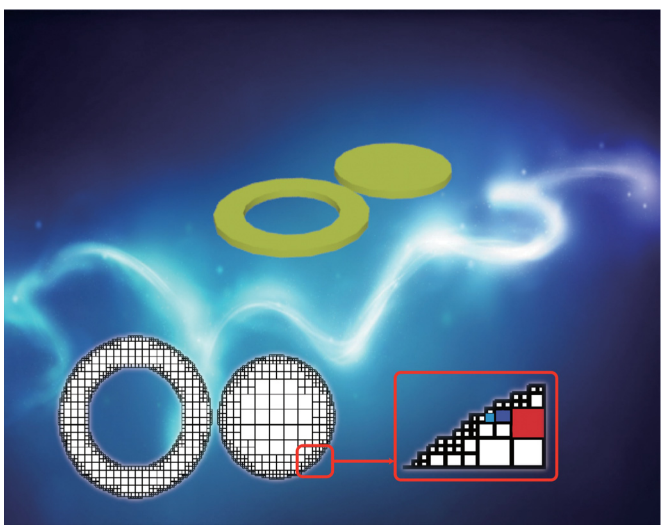

DOI: 10.1109/JPHOT.2012.2185222

Volumetric Method of Moments and Conceptual Multilevel Building Blocks for Nanotopologies

X. Zheng,[1] V. K. Valev,[2] N. Verellen,[2,3] Y. Jeyaram,[2] A. V. Silhanek,[2,4] V. Metlushko,[5] M. Ameloot,[6] G. A. E. Vandenbosch,[1] *Senior Member, IEEE*, and V. V. Moshchalkov[2]

[1]ESAT-TELEMIC, Katholieke Universiteit Leuven, 3001 Leuven, Belgium
[2]INPAC, Katholieke Universiteit Leuven, 3001 Leuven, Belgium
[3]IMEC, 3001 Leuven, Belgium
[4]Départment de Physique, Université de Liège, Liège 4000, Belgium
[5]Department of Electrical and Computer Engineering, University of Illinois at Chicago, Chicago, IL 60607 USA
[6]University Hasselt and Transnational University Limburg, BIOMED, Diepenbeek, Belgium

DOI: 10.1109/JPHOT.2012.2185222
1943-0655/$31.00 ©2012 IEEE

Manuscript received January 12, 2012; accepted January 15, 2012. Date of publication January 23, 2012; date of current version February 10, 2012. This work was supported by the Fund for Scientific Research-Flanders (FWO-V), the Katholieke Universiteit Leuven (GOA), Methusalem Funding by the Flemish government, the Belgian Interuniversity Attraction Poles Program, and by the U.S. National Science Foundation (NSF) under Grant ECCS-0823813 (VM). This work was also supported by the NSF through the NSF ERC Center for Extreme Ultraviolet Science and Technology under NSF Award EEC-0310717. Corresponding author: X. Zheng (e-mail: xuezhi.zheng@esat.kuleuven.be).

Abstract: On the basis of the relationship between charge dimensionality and singular field behavior, it is proven that in a volumetric description of a volume current carrying topology, half rooftops of different binary hierarchical level are allowed without introducing numerical difficulties. This opens the possibility to use a very efficient multilevel hierarchical meshing scheme in a volumetric method-of-moments (V-MoM) algorithm. The new meshing scheme is validated by numerical calculations and experiments. It paves the way toward a much more efficient use of MoM in the description of arbitrarily shaped nanostructures at infrared and optical frequencies.

Index Terms: Method of moments (MoM), nanostructures, plasmonics, optical frequencies.

1. Introduction

In the last decade, the study of the interaction between light and nanostructures has drawn a lot of attention from both the physics and the engineering communities. Topologies very familiar to microwave antenna designers, like monopole [1], dipole [2], and Yagi-Uda configurations [3], are extensively studied at optical frequencies since their characteristics at microwave and optical frequencies are similar. This similarity can be used to speed up the design of such structures in the optical range.

However, there exists a fundamental difference. At microwave frequencies, the skin depth of the metals used is extremely small compared with the dimensions of the structure: several orders of magnitude. This means that they can be treated as structures carrying 2-D surface currents, and the concept of surface impedance can be adopted. On the other hand, at optical frequencies, the skin depth is comparable with the thickness of the nanostructures. Consequently, the current flowing in the structure is a 3-D one. Any modeling scheme considered for these structures has to cope with this.

The traditional numerical techniques used in the microwave community are now being explored in the field of nanotechnology. Although most researchers use the differential approach, for example FDTD in [4]–[6], several great advantages of the method of moments (MoM) in comparison with the FEM and FDTD method should not be ignored. The first one is that only the current carrying components have to be discretized. The complex environment, which may include multilayered substrates, is taken into account via Green's functions. The discretized components are modeled in terms of equivalent currents. These currents fill completely all metal/dielectric volumes, and the boundary conditions are satisfied in an average sense inside these volumes, on surfaces, or lines, depending on the selected testing procedure. The result is that MoM is intrinsically faster than the two other methods. The second advantage of the MoM technique is that, if properly formulated, it is variationally stable since most of the output parameters are expressed in integral form over the equivalent currents. As a consequence even if the calculated currents differ considerably from the exact solution, integral parameters over both currents may remain very similar. Further, this will be illustrated by showing that even with a rather rough mesh high-quality physical results may be obtained. A third advantage is that MoM does not heavily suffer from field singularities near sharp edges, since they are analytically incorporated inside the Green's functions. For the FEM and the FDTD method, special care (=fine mesh) should be taken to correctly describe these field singularities [7]. For these reasons, there are a few groups that have used the MoM to solve the integral equations describing the structure [8]–[11]. It can be proven that MoM can be implemented in a very efficient way for plasmonic nanostructures [12].

The modeling group around Martin [8], [9] uses surface integral equations, where the boundaries of the plasmonic structures are discretized. This is a classical technique, well known in the microwave community. Another possibility is to use the volumetric equivalence principle. The nanoparticles are replaced by the equivalent induced electric polarization currents, and the volumetric integral equations describing the structure are subsequently solved by the MoM. As a consequence of the fact that only surface currents have to be described at the microwave frequencies, this technique is rarely used in the microwave community. To the knowledge of the authors, this approach was introduced to the plasmonics community in [11] and [12].

At microwave and millimeter wave frequencies, in a MoM algorithm the surface current is modeled with subdomain basis functions defined over two adjacent segments, i.e., a full rooftop is formed out of two half rooftops in a seamless manner. It is impossible to work with the half rooftops separately, since this would invoke the appearance of unphysical line charges accumulating at the segment boundaries, consequently introducing singularities in the induced electric field. It can be shown that this seriously compromises the stability of any MoM implementation.

In this paper, volumetric MoM (V-MoM) is considered. Three-dimensional full rooftops are introduced as a natural extension of their 2-D counterparts. However, half rooftops are used as well. In V-MoM, their use is permitted because 3-D half rooftops do not generate line charge densities but surface charge densities, which do not cause any singularities. This observation is the core point of this paper. Moreover, on the ground of this observation, it is worthwhile to investigate the possibility of using half rooftops in a hierarchical meshing scheme, making use of smaller and smaller hexahedral or tetrahedral blocks, in order to describe the details at the boundaries of complex 3-D structures with a higher resolution. It will be proven that this boosts the computational efficiency of the MoM implementation considerably.

This work is organized as follows. First, we briefly overview the well-known relationships between the dimensionality of a charge density and the (possibly) singular behavior of the induced electric field and the stored electric energy density. The line of reasoning given clearly explains why half rooftops cannot be used at microwave and millimeter-wave frequencies. The observation that, in the case of structures at IR and optical frequencies, a volumetric current description can be used, is the basis inspiring the idea of using half 3-D rooftops to construct a very efficient hierarchical meshing scheme. In order to validate the new meshing scheme, two structures are studied: a so-called Ring Near Disc Cavity (RNDC) structure and a Plates–Wire (PW) structure. The RNDC is

TABLE 1

Overview of S' and B' for different cases

Type of Source Current	Type S'	Type B'	Dimension Charge on B'
Volume Current	Volume	Surface	2D
Surface Current	Surface	Line	1D
Line Current	Line	End points of line	0D

analyzed in the far field by both MoM and FDTD with different meshes. The charge and electric field distributions of the PW structure are studied with MoM. Numerical calculations are compared with measurements.

2. Charge Density and Electric Field Behavior

In general, the electric field can be expressed in terms of a scalar potential ϕ and a vector potential $\mathbf{A}$. In the frequency domain, with the Lorentz gauge imposed, the electric field in free space is

$$\mathbf{E} = -j\omega\mathbf{A} - j\frac{1}{\omega\mu_0\epsilon_0}\nabla(\nabla\cdot\mathbf{A}) \tag{1}$$

where ω is the angular frequency. The vector potential in free space due to a current $\mathbf{J}$ is

$$\mathbf{A}(\mathbf{r}) = \frac{\mu_0}{4\pi}\int_{S'}\mathbf{J}(\mathbf{r})g(\mathbf{r},\mathbf{r}')\,dS' \tag{2}$$

with $g(\mathbf{r},\mathbf{r}')$ the free space Green's function $(e^{-jk|r-r'|}/4\pi|r-r'|)$, with the wavenumber k, and r and r' the observation and source point. Equation (1) is integrated over the source region S'. Substituting (2) into (1) and using standard mathematical manipulations, for example interchanging the order of the integral and the gradient, we arrive at

$$\mathbf{E}(\mathbf{r}) = -j\omega\mu_0\int_{S'}g(\mathbf{r},\mathbf{r}')\mathbf{J}(\mathbf{r}')dS' - \frac{1}{\epsilon_0}\nabla\int_{S'}g(\mathbf{r},\mathbf{r}')\left(\frac{\nabla\cdot\mathbf{J}(\mathbf{r}')}{-j\omega}\right)dS' - \frac{1}{\epsilon_0}\nabla\oint_{B'}g(\mathbf{r},\mathbf{r}')\left(\frac{\mathbf{n}\cdot\mathbf{J}(\mathbf{r}')}{-j\omega}\right)dB'. \tag{3}$$

Note that the integral in the last term of (3) is conducted over the (closed) boundary B' surrounding the source region, which is one dimension lower than the integral domain of the first two terms. n is the unit vector normal to the boundary B'. $\left(\frac{\mathbf{n}\cdot\mathbf{J}(\mathbf{r}')}{-j\omega}\right)$ represents the charge accumulation on the boundary due to the normal current arriving there. The general expression for the contribution of a charge ρ to the scalar potential can thus be written as

$$\int_{\text{source}}\frac{e^{-jk|r-r'|}}{|r-r'|}\rho\,d(\text{source}) \tag{4}$$

where the source domain can be 3-D, 2-D, 1-D, or 0-D (a point), depending on the situation. An overview of the type of source current and the type of boundary charge can be found in Table 1.

When an observation point approaches a source point, the Green's function factor in (4) reduces to

$$\lim_{\mathbf{r}\to\mathbf{r}'}\frac{e^{-jk|\mathbf{r}-\mathbf{r}'|}}{|\mathbf{r}-\mathbf{r}'|} = \lim_{\mathbf{r}\to\mathbf{r}'}\frac{1-jk|\mathbf{r}-\mathbf{r}'|-k^2|\mathbf{r}-\mathbf{r}'|^2}{|\mathbf{r}-\mathbf{r}'|} = \lim_{\mathbf{r}\to\mathbf{r}'}\frac{1}{|\mathbf{r}-\mathbf{r}'|} - jk + O(\mathbf{r}-\mathbf{r}'). \tag{5}$$

This represents a singularity of order 1. This means that in the general expression (4), an integration over a surface is necessary in order to keep the scalar potential and, thus, the energy stored in the electric field generated by the charge, finite in the immediate neighborhood of the source.

TABLE 2

Types of singularity for different charge dimensionalities. r is the distance to the charge on B which has to be considered in the limit to zero

Boundary B	Electric Field	Electric Field Density	Energy in dV around B
Surface (2D)	No Singularity	No Singularity	No Singularity
Line (1D)	$\sim \frac{1}{r}$	$\sim \frac{1}{r^2}$	$\sim log(r)$
Point (0D)	$\sim \frac{1}{r^2}$	$\sim \frac{1}{r^4}$	$\sim \frac{1}{r}$

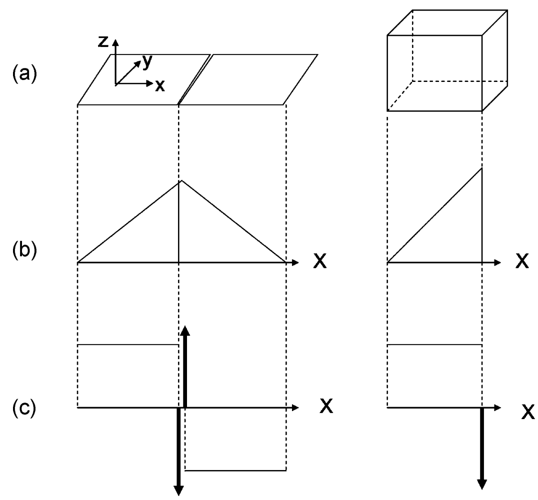

Fig. 1. (a) Paired 2-D segments and stand-alone 3-D segment. (b) 2-D full rooftop and 3-D individual half rooftop, current as a function of x. (c) Charge distribution as a function of x on paired 2-D segments and stand-alone 3-D segment; the arrows represent Dirac pulses.

Consequently, both for a point charge (no integration) and for a line charge (1-D integration), the electric field is singular, and the electric energy density goes to infinity in the neighborhood of the source region. In classical electrodynamics, this is an unphysical situation which cannot occur in practice (see Table 2).

3. Use of Half Rooftop Basis Functions

The last observation of the previous section can be considered a physical reason why, for 2-D surface currents, 2-D half rooftop basis functions must always be defined in pairs to form full rooftop basis functions. In this way, the singularity generated by the line current accumulating at the current carrying side of the half rooftop is rigorously compensated by an opposite singularity due to the connected half rooftop. Pairing half rooftops with different sizes (see Fig. 1) is also forbidden. Also, in this case, unphysical line charges accumulate, leading to unphysical singularities in the field and electric energy densities.

At IR and optical frequencies, the skin depth is of the same order as the thickness of the nanostructures, which is normally around a few tens of nanometers. This makes the nanostructures 3-D current carrying structures. Consequently, the physical reason that prohibits use of half rooftops at lower frequencies is not there any more. The surface charges resulting from 3-D half rooftops do not generate any physical anomalies. This observation was the main inspiration for the idea to investigate a hierarchical use of 3-D half rooftops in a binary scheme; see Fig. 2. At the edges of a structure, the actual boundary is reconstructed with an increased resolution by adding blocks, where necessary, that are half the size of the blocks of the previous level. In Fig. 2, for example, there are three levels. The blocks of level 1 are used throughout the interior of the structure. At the

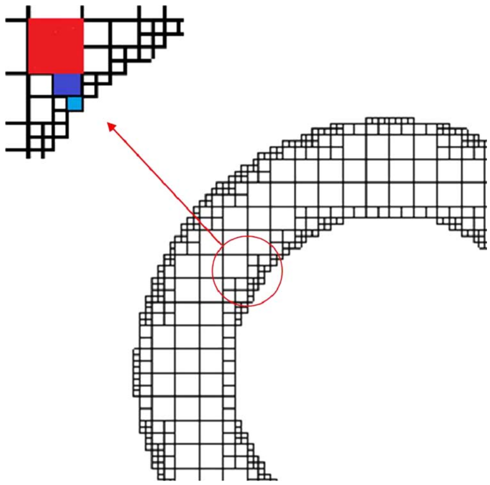

Fig. 2. Hierarchical use of 3-D half rooftops in a binary scheme. Red: level 1; blue: level 2; light blue: level 3.

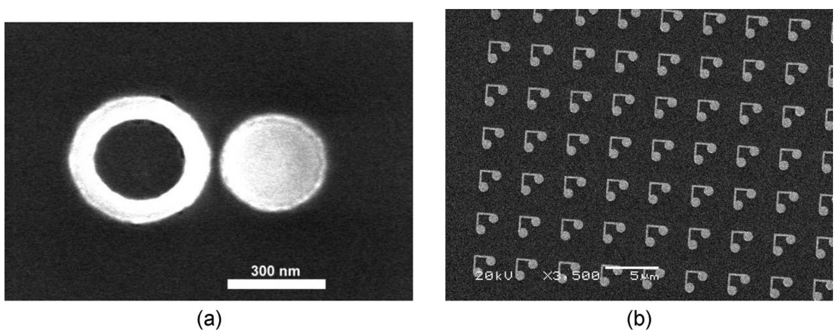

Fig. 3. SEM image of RNDC and PW. (a) SEM image of RNDC. (b) SEM image of PW.

boundary, they are supplemented by blocks of level 2, with half the size of the blocks of level 1, and blocks of level 3, with half the size of the blocks of level 2, etc.

4. Numerical Results

In this section, the proposed technique is illustrated and validated for two nanostructures: RNDC [see SEM in Fig. 3(a)] and PW [see SEM in Fig. 3(b)]. The new meshing scheme was implemented within our in-house developed MoM tool MAGMAS [13]–[16]. The validation is also achieved through a comparison with the FDTD solver Lumerical [17], which is widely used in the optical and photonics research community.

4.1. RNDC

This structure was first described in [4] and first analyzed with a coarse MoM mesh in [12]. The parameters defining the geometry are tabulated in Table 3.

The structure is made of gold and is situated on top of a glass substrate with refractive index 1.5. As a consequence of the etching process, the sidewalls of the structure are 20° slanted. In the experiment, transmission spectra were taken with a Fourier transform infrared (FTIR) microscope (Bruker Vertex 80v + Hyperion). The incident light from a tungsten lamp is focused on the sample via a 15 magnification, NA = 0.4 reflective Cassegrain condenser and collected in transmission with an identical objective. This type of objective creates a light cone with angles between 9.8° and 23.6°

TABLE 3

Parameters defining the structure

Description	Value
Disc Diameter	325nm
Ring Outer Diameter	425nm
Ring Width	80nm
Ring-Disc Separation	20nm
Thickness of RNDC	20nm

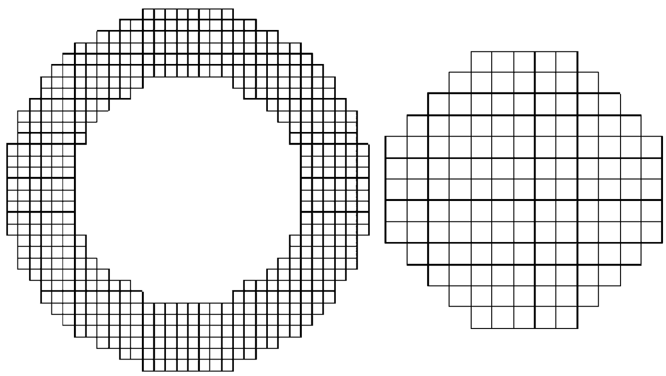

(a)

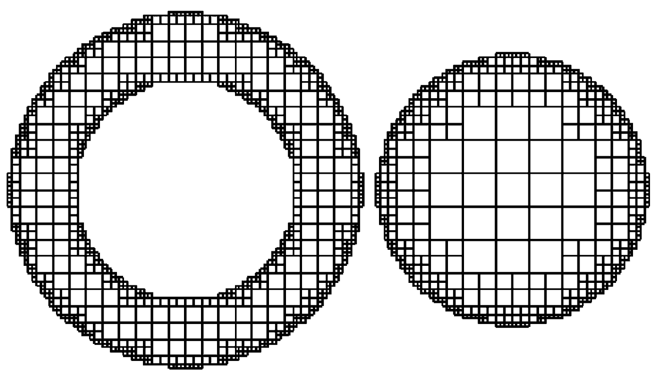

(b)

Fig. 4. Meshes used for the RNDC structure. (a) Mesh 1: uniform coarse mesh for both components. (b) Mesh 2: binary hierarchical mesh with three levels for ring and four levels for disc.

impinging on the sample surface. The resulting k-vector spread leads to an experimental angle of incidence, which is not uniquely defined. The transmitted light is then polarized, spatially filtered with a metal knife edge aperture, and detected with a liquid nitrogen cooled mercury-cadmium-telluride (MCT) and Si diode detector. All spectra are normalized with respect to a reference spectrum taken on the bare substrate under identical conditions [18].

In the FDTD simulations with Lumerical, the structure is modeled with 2.5 nm side cubes within a $2.5 \times 2.5 \times 0.75$ μm box. The far field boundary condition is a Perfectly Matched Layer (PML), ensuring a negligible reflection. The excitation is a plane wave. The extinction cross section is calculated by Lumerical using the built-in applet. It is worth noticing that the 20° slanted side walls are also considered in Lumerical. In MAGMAS, a plane wave is used as excitation. Two meshes are used, i.e., a coarse uniform one and a fine one; see, Fig. 4. In order to compare FDTD and V-MoM simulation results with the experiments, all the extinction cross sections from the simulations are normalized with respect to the ones obtained from the measurements; see Figs. 5, 6, 10, and 11.

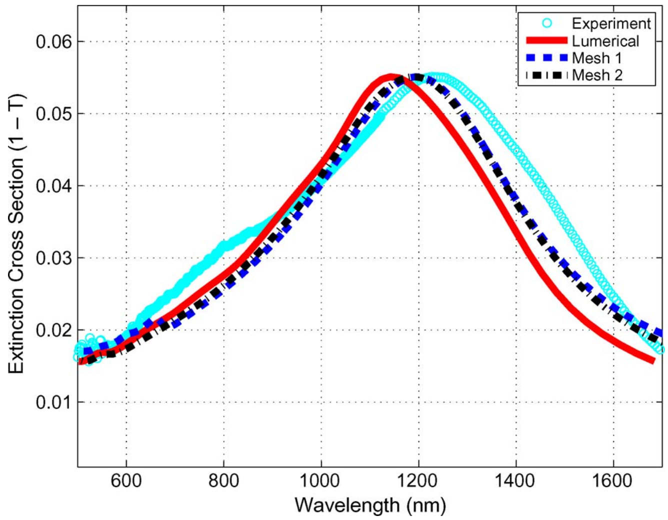

Fig. 5. Extinction cross section of the isolated disk structure.

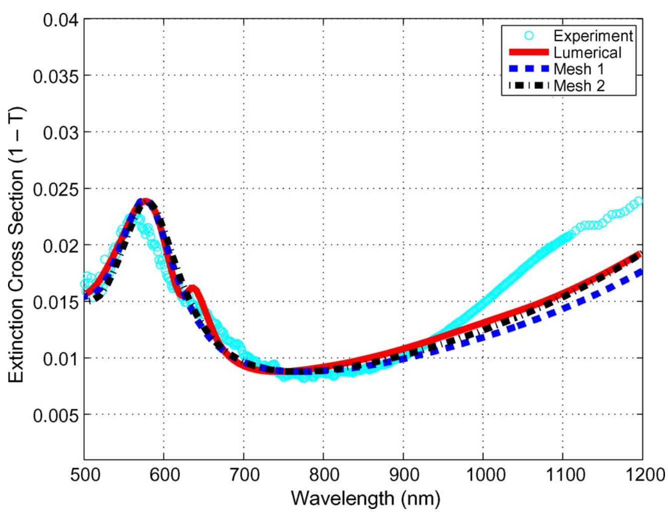

Fig. 6. Extinction cross section of isolated ring structure.

Fig. 5 shows the extinction cross section of an isolated single disk, excited by horizontally polarized (X polarized) light from the bottom. A similar behavior is observed for Lumerical, MAGMAS meshes 1 and 2, and measurements. A noticeable kink appears at short wavelengths around 700 nm for mesh 1. This is due to the fact that mesh 1 gives a poor description of the circumference of the disc. Further, there are two differences between the FDTD and MoM simulations. The first one is that the FDTD simulation is blue-shifted with respect to the MoM one. The second one is that the width of the peak in the FDTD simulation is broader than the one with MoM. Both facts can be explained by the slanted edges, and not taken into account in the MoM solver.

Fig. 6 depicts the extinction cross section of an isolated ring structure illuminated by X polarized light. Meshes 1 and 2 are used in the MAGMAS simulations. At short wavelengths, all simulations agree with each other. At long wavelengths, a discrepancy appears between the simulations and the measurements.

It is absolutely crucial to point out the following. In case the hierarchical meshing is performed in an improper way, erroneous results may occur. This is illustrated in Fig. 8 where an unphysical

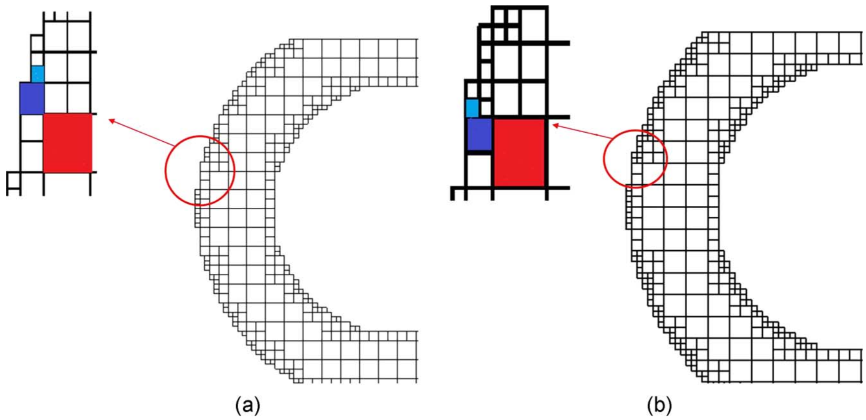

Fig. 7. Improper and proper meshes used for the ring structure. Red: level 1; blue: level 2; light blue: level 3. (a) Mesh 3, improper mesh used for the ring structure, and creating a spike in the extinction cross section of Fig. 8. (b) Proper mesh used for the ring structure.

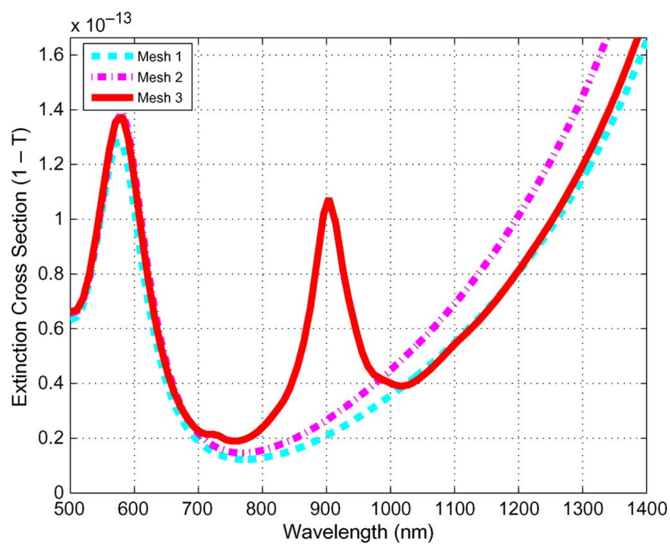

Fig. 8. Extinction cross section of the isolated ring structure.

spike occurs around 900 nm for a mesh 3 given in Fig. 7(a). In Fig. 7(a), the medium-size block marked in blue is not paired with the two smallest size blocks (light blue), as in Fig. 7(b). The resultant erroneous spike does not occur for meshes 1 and 2, nor in the Lumerical results (see Fig. 8). The relation of this spike with the characteristics of mesh 3 was investigated in more detail.

The charge distribution on the top surface and the induced electric current evaluated at three fourths of the height are shown at 900 nm (330 THz) for mesh 2 and 3 in Fig. 9(a)–(d). In Fig. 9(a), the expected dipolar mode is clearly seen in the distributions. However, for mesh 3, this dipolar mode is seriously distorted by local erroneous charge accumulations, as can be seen in Fig. 9(b). The problem can easily be explained by looking at the set of blocks in the red circle in Fig. 7. It is seen that the level 2 block there has a boundary surface (the one at the right), which is only partially exposed to the outside. The other part is covered by a block of level 3. Since, physically, there are no surface charges inside the volume, this means that the surface charge generated by the half rooftop corresponding to this right surface has to be compensated by the surface charge of the half rooftop of the level 3 covering block. At the same time, this half rooftop has to model the

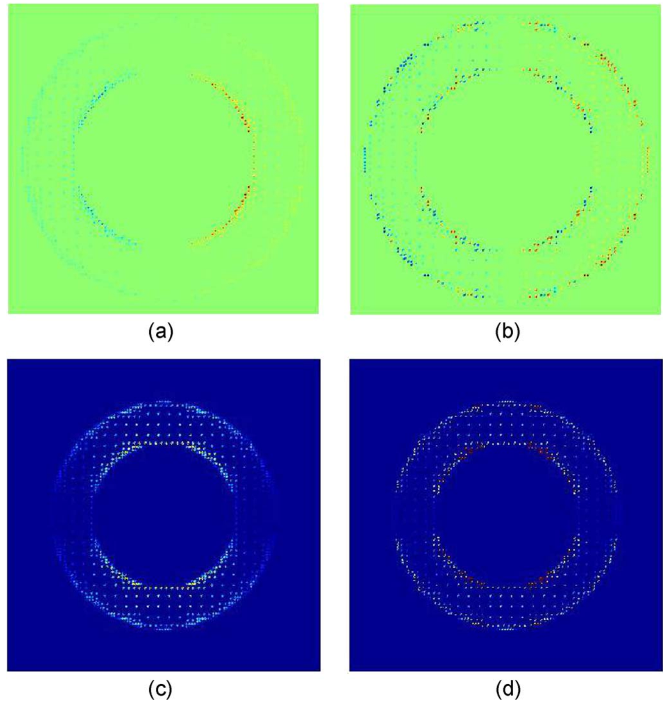

Fig. 9. Surface charge and volume current distribution. (a) Surface charge distribution for mesh 2. (b) Surface charge distribution for mesh 3. (c) Volume current distribution for mesh 2. (d) Volume current distribution for mesh 3.

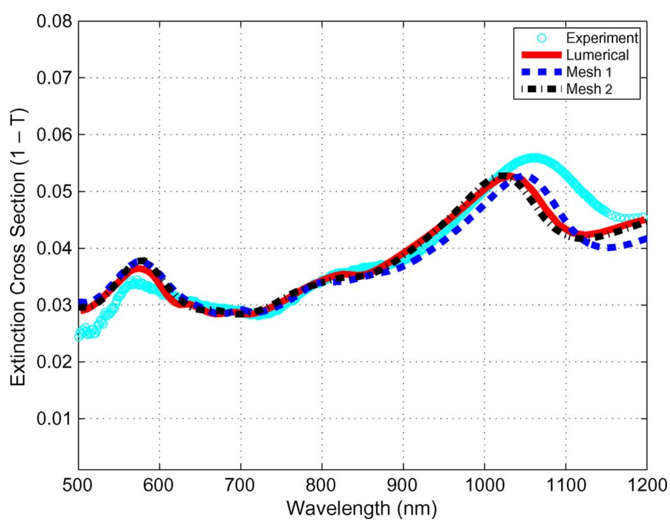

Fig. 10. Extinction cross section of RNDC with X polarization.

surface charge that is physically present at the part exposed to the outside. This set of two contradictory requirements causes the unphysical charge distribution wherever such a situation occurs. In mesh 2, this problem does not occur since boundary surfaces are either completely exposed or not exposed to the outside.

In Fig. 10, the response of the total RNDC structure excited by X polarized light is given. At short wavelengths, all meshes give more or less the same result. A slight deviation from the measurements can be seen. In the middle range, all the simulations show good correspondence, also

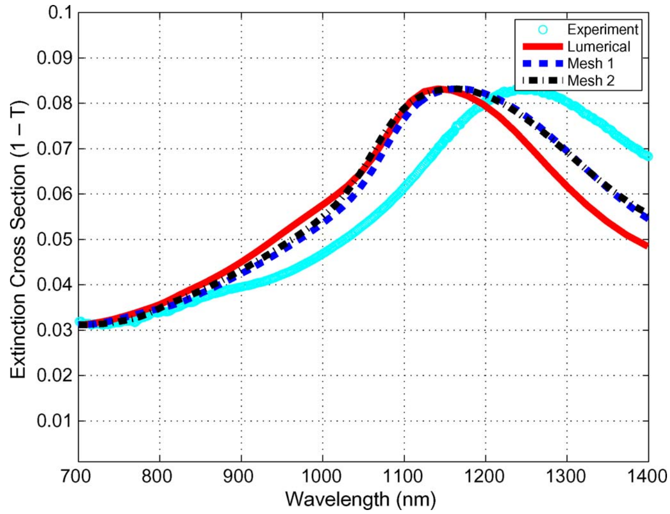

Fig. 11. Extinction cross section of RNDC with Y polarization.

TABLE 4

Parameters defining the structure

Parameter	Value
Plate Diameter	800nm
Wire Width	200nm
Wire Length (see red arrow in Fig.)	1.2um
Structure Periodicity	4um
Thickness of the structure	25nm

with the measurements. At long wavelengths, starting around 800 nm, the coarse mesh starts to loose track compared with the other two simulations. Lumerical and mesh 2 keep matching the measurements up to 1000 nm.

For Y polarized light (see Fig. 11), all the simulations show a good correspondence at short wavelengths. Starting around 850 nm, the measurement starts to deviate from the simulations.

Last but not the least, discrepancies between simulations and experiments are observed in Figs. 5, 6, 10, and 11. To explain these differences, we have to notice that the experimental dimensions of the nanostructures are estimated from the SEM images, and it is difficult to obtain these with an accuracy better than 10 nm. Moreover, it is a well-known fact that the material properties at the surface of the gold nanostructures can deviate from the bulk values due to surface defects and grain boundaries. Spectral shifts and fluctuations in absolute extinction cross section can easily be explained from this. Again, imperfect fabrication processes cause problems. For example, the larger discrepancy between Y and X polarization in Figs. 10 and 11 could directly result from a small asymmetry in the disk and/or ring particle. Therefore, the overall spectral shape of the measurements should correspond to the simulated spectra, not necessarily the exact spectral position of the resonances.

4.2. PW

The PW structure is made of gold on top of a SiO_2/Si substrate. The parameters defining the geometry are listed in Table 4. In the experiment, its near-field behavior is captured by Second Harmonic Imaging Microscopy (SHG microscopy) [19]–[22]. SHG microscopy is performed with an LSM 510 META scanning confocal microscope from Zeiss. The light source for this microscope is a femtosecond pulses Ti:Sapphire laser at a wavelength of 800 nm. The laser passes through a dichroic mirror (HFT KP650) and is focused on the sample surface by an alpha PLAN-apochromat

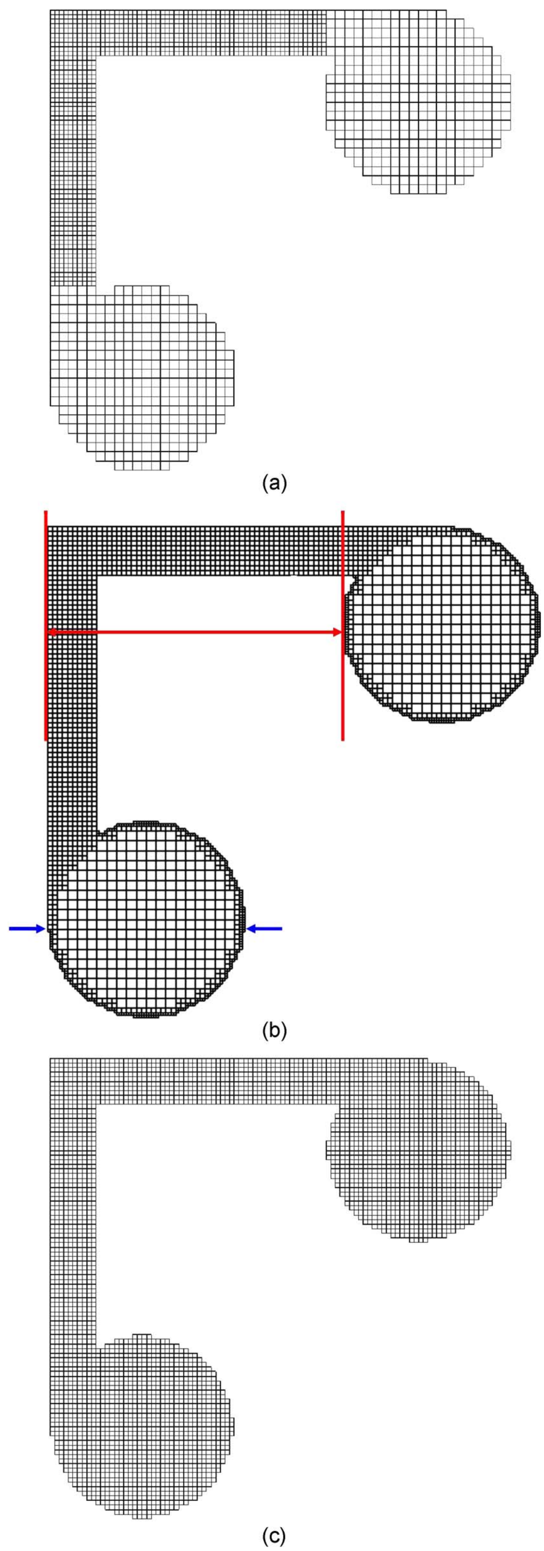

Fig. 12. Meshes used for PW structure. (a) Uniform coarse mesh for both PW. (b) Mesh with three levels for the PW structure. (c) Uniform fine mesh for the PW structure.

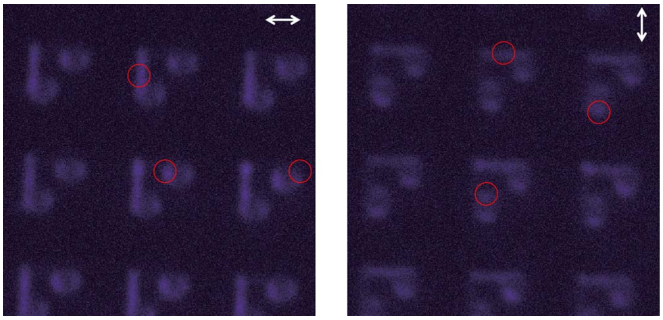

Fig. 13. SHG microscopy result for (a) X polarized light and (b) Y polarized light (hotspots are marked by red circles).

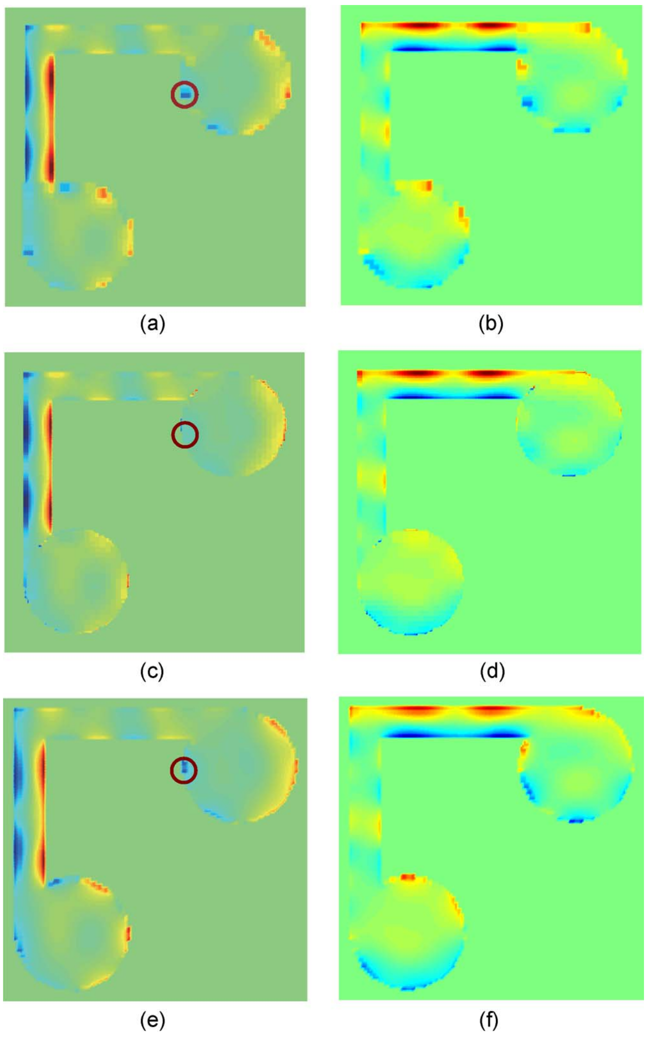

Fig. 14. Charge distribution on the surface. The polarity is coded with blue and red, i.e., more red with more positive charge, and more blue with more negative charge. (a) X polarized light with mesh of Fig. 12(a). (b) Y polarized light with mesh of Fig. 12(a). (c) X polarized light with mesh of Fig. 12(b). (d) Y polarized light with mesh of Fig. 12(b). (e) X polarized light with mesh of Fig. 12(c). (f) Y polarized light with mesh of Fig. 12(c).

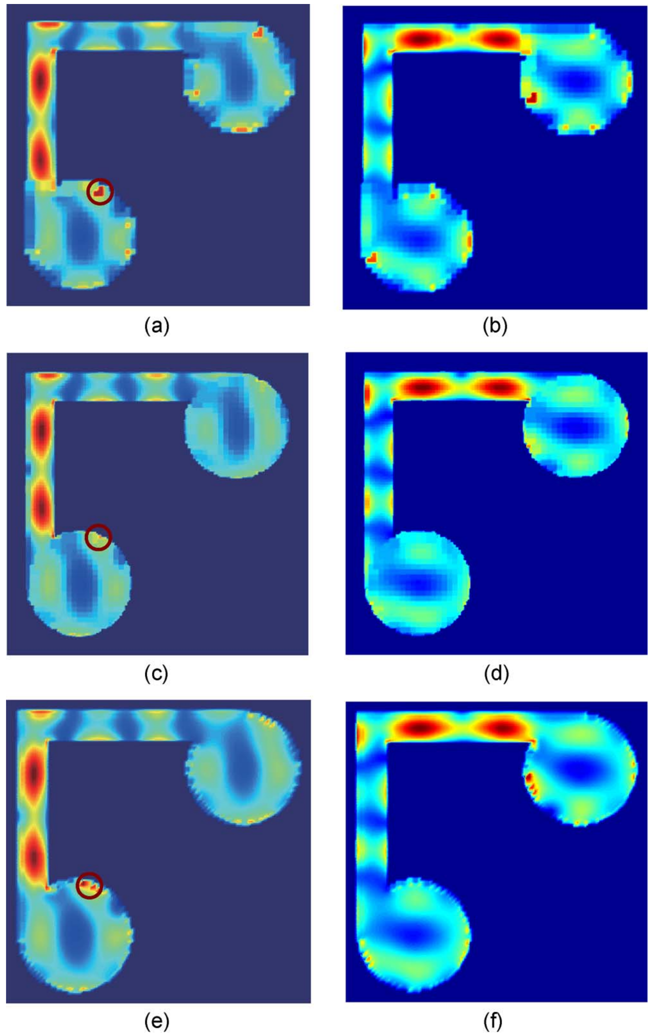

Fig. 15. Magnitude of electric field in PW. The magnitude is coded from blue to red. (a) X polarized light with mesh of Fig. 12(a). (b) Y polarized light with mesh of Fig. 12(a). (c) X polarized light with mesh of Fig. 12(b). (d) Y polarized light with mesh of Fig. 12(b). (e) X polarized light with mesh of Fig. 12(c). (f) Y polarized light with mesh of Fig. 12(c).

100× oil objective with numerical aperture of 1.46. After frequency conversion by the nanostructures, the second harmonic 400 nm light is separated from the fundamental 800 nm by reflection on the dichroic mirror. Further filtering is ensured by a short-pass filter (KP 685) before collection by a photomultiplier tube.

In MAGMAS, the structure is modeled by a coarse mesh, a hierarchical mesh with three levels, and a uniform fine mesh; see Fig. 12. In the simulation, the structure is built on a layer of SiO2 with 100 nm thickness on top of a half space of Silicon substrate. The other half space is air. The structure is illuminated by X (horizontal) and Y (vertical) polarized light.

Measurements obtained with SHG microscopy are given in Fig. 13. Two hotspots are observed in each plate. For the X polarization, the hotspots align along the horizontal direction. For the Y polarization, they align along the vertical direction. Moreover, the vertical wires brighten up when excited by the X polarized light, while the horizontal wires brighten up when excited by the Y polarized light.

The surface charge distributions simulated by MAGMAS and the resultant electric field distributions are shown in Figs. 14(a)–(f) and 15(a)–(f), respectively. For all meshes in Fig. 12, on the

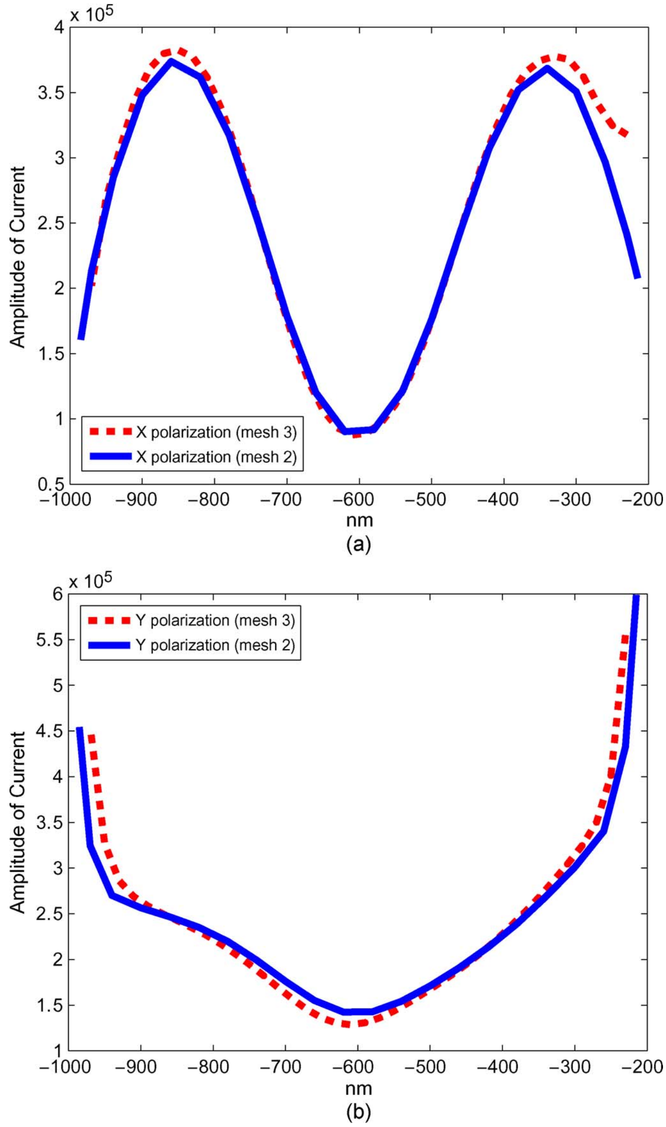

Fig. 16. One-dimensional cross-sectional plot of magnitude of electric field in PW. (a) X polarization. (b) Y polarization.

connection wires, X and Y polarized light drives positive and negative charges away from each other. They accumulate at the edges of this nanostructure. The charges form dipole-like distributions, in this way exciting the hotspots seen with SHG microscopy. On the plate, the relatively large size allows the propagation of a surface plasmon, which subsequently forms a standing wave pattern due to the finite size of the structure. On the plates, as shown in Figs. 12 and 13, due to the rough staircase modeling with the coarse mesh, the surface charge distribution and the induced electric field show unphysical sharp peaks at the circumference and in the corners between connection wires and plates (see red circles in Figs. 14 and 15).

In order to further compare the uniform fine mesh [see Fig. 12(c)] and the mesh with three levels [see Fig. 12(b)], we make a cut at the position of the blue arrows in Fig. 12(b) in the bottom plate and plot the variation of the electric field along the horizontal axis in Fig. 16. Both Fig. 16(a) and (b) show that in the center of the plate the electric fields resulting from different meshes almost coincide with each other, but at the boundaries, they show some minor differences, which is the direct result of describing the boundary with blocks with different sizes.

TABLE 5

Number of unknowns, memory cost, and computational time with Intel Xeon CPU 7550 with 128 GB memory

Meshing	Number of Unknowns	Memory Cost (Gigabytes)	Inversion Time (in seconds)
Fig. (12a)	12710	3.2	225
Fig. (12b)	20456	6.6	955
Fig. (12c)	26192	11	1966

The number of unknowns, the memory cost, and the computational time, for the three meshes, are given in Table 5. It is clearly seen that the mesh in Fig. 12(c) generates the largest number of unknowns, i.e., 26 192, leads to the largest amount of memory, i.e., around 11 Gigabytes, and takes the longest time to finish the computation. However, the results are of the same quality as the results for the mesh in Fig. 12(b), which is computationally much more effective.

5. Conclusion

Within the framework of a V-MoM algorithm, a meshing scheme using a binary hierarchical mesh with multiple levels is introduced and investigated. It is shown that with the new meshing technique, a high resolution and accuracy can be combined without compromising calculation times. The technique uses the concept of half rooftops, which is concept that is not applicable for structures in the microwave and millimeter-wave range.

References

[1] T. H. Taminiau, F. B. Segerink, R. J. Moerland, L. K. Kuipers, and N. F. van Hulst, "Near-field driving of a optical monopole antenna," *J. Opt. A, Pure Appl. Opt.*, vol. 9, no. 9, pp. S315–S321, Sep. 2007.
[2] P. Muhlschlegel, H.-J. Eisler, O. Martin, B. Hecht, and D. Pohl, "Resonant optical antennas," *Science*, vol. 308, no. 5728, pp. 1607–1609, Jun. 2005.
[3] D. Dregely, R. Taubert, J. Dorfmuller, R. Vogelgesang, K. Kern, and H. Giessen, "3D optical Yagi-Uda nanoantenna array," *Nat. Commun.*, vol. 2, no. 267, p. 1268, Apr. 2011.
[4] N. Verellen, Y. Sonnefraud, H. Sobhani, F. Hao, V. Moshchalkov, P. V. Dorpe, P. Nordlander, and S. A. Maier, "Fano resonances in individual coherent plasmonic nanocavities," *Nano Lett.*, vol. 9, no. 4, pp. 1663–1667, Apr. 2009.
[5] R. Kappeler, D. Erni, C. Xudong, and L. Novotny, "Field computations of optical antennas," *J. Comput. Theor. Nanosci.*, vol. 4, no. 3, pp. 686–691, May 2007.
[6] R. Qiang, R. L. Chen, and J. Chen, "Modeling electrical properties of gold films at infrared frequency using FDTD method," *Int. J. Infrared Millim. Waves*, vol. 25, no. 8, pp. 1263–1270, Aug. 2004.
[7] F. P. G. de Arquer, V. Volski, N. Verellen, G. A. E. Vandenbosch, and V. V. Moshchalkov, "Engineering the input impedance of optical nano dipole antennas: Materials, geometry and excitation effect," *IEEE Trans. Antennas Propag.*, vol. 59, no. 9, pp. 3144–3153, Sep. 2011.
[8] B. Gallinet and O. J. Martin, "Scattering on plasmonic nanostructures arrays modeled with a surface integral formulation," *Photon. Nanostruct. Appl.*, vol. 8, no. 4, pp. 278–284, Sep. 2010.
[9] A. M. Kern and O. J. Martin, "Surface integral formulation for 3D simulations of plasmonic and high permittivity nanostructures," *J. Opt. Soc. Amer.*, vol. 26, no. 4, pp. 732–740, Apr. 2009.
[10] J. M. Taboada, J. Rivero, L. Landesa, M. G. Araujo, F. Obelleiro, and O. Rubinos-Lopez, "Method of moments formulation for the analysis and design of plasmonic nano-optical antennas of arbitrary shape," in *Proc. 5th EUCAP*, pp. 2205–2208.
[11] G. A. E. Vandenbosch, V. Volski, N. Verellen, and V. V. Moshchalkov, "The method of moments at IR and optical frequencies," in *Proc. iWAT*, 2011, pp. 10–13.
[12] G. A. E. Vandenbosch, V. Volski, N. Verellen, and V. V. Moshchalkov, "On the use of the method of moments in plasmonic applications," *Rad. Sci.*, vol. 46, p. RS0E02, May 2011, DOI:10.1029/2010RS004582.
[13] Y. Schols and G. A. E. Vandenbosch, "Separation of horizontal and vertical dependencies in a surface/volume integral equation approach to model quasi 3-D structures in multilayered media," *IEEE Trans. Antennas Propag.*, vol. 55, no. 4, pp. 1086–1094, Apr. 2007.
[14] G. A. E. Vandenbosch and A. R. Van de Capelle, "Mixed-potential integral expression formulation of the electric field in a stratified dielectric medium," *IEEE Trans. Antennas Propag.*, vol. 40, no. 7, pp. 806–817, Jul. 1992.
[15] F. J. Demuynck, G. A. E. Vandenbosch, and A. R. Van de Capelle, "The expansion wave concept, part I: Efficient calculation of spatial green's functions in a stratified dielectric medium," *IEEE Trans. Antennas Propag.*, vol. 46, no. 3, pp. 397–406, Mar. 1998.
[16] M. Vranken and G. A. E. Vandenbosch, "Hybrid dyadic-mixed-potential and combined spectral-space domain integral equation analysis of quasi-3-D structures in stratified media," *IEEE Trans. Microw. Theory Tech.*, vol. 51, no. 1, p. 216225, Jan. 2003.

[17] [Online]. Available: http://www.lumerical.com

[18] N. Verellen, P. V. Dorpe, D. Vercruysse, G. A. E. Vandenbosch, and V. V. Moshchalkov, "Dark and bright localized surface plasmons in nanocrosses," *Opt. Exp.*, vol. 19, no. 12, pp. 11 034–11 051, Jun. 2011.

[19] V. K. Valev, A. V. Silhanek, Y. Jeyaram, D. Denkova, B. D. Clercq, V. Petkov, X. Zheng, V. Volskiy, W. Gillijns, G. A. E. Vandenbosch, O. A. Aktsipetrov, M. Ameloot, V. V. Moshchalkov, and T. Verbiest, "Hotspot decorations map plasmonic patterns with the resolution of scanning probe technique," *Phys. Rev. Lett.*, vol. 106, no. 22, p. 226803, Jun. 2011.

[20] V. K. Valev, X. Zheng, C. Biris, A. Silhanek, V. Volskiy, B. D. Clercq, O. Aktsipetrov, M. Ameloot, N. Panoiu, G. A. E. Vandenbosch, and V. Moshchalkov, "The origin of second harmonic generation hotspots in chiral optical metamaterials," *Opt. Mater. Exp.*, vol. 1, pp. 36–45, 2011.

[21] V. K. Valev, A. V. Silhanek, B. D. Clercq, W. Gillijns, Y. Jeyaram, X. Zheng, V. Volskiy, O. A. Aktsipetrov, G. A. E. Vandenbosch, M. Ameloot, V. V. Moshchalkov, and T. Verbiest, "U-shaped switches for optical information processing at the nanoscale," *Small*, vol. 7, no. 18, pp. 2573–2576, Sep. 2011.

[22] V. K. Valev, B. D. Clercq, X. Zheng, D. Denkova, E. J. Osley, S. Vandendriessche, A. V. Silhanek, V. Volskiy, P. A. Warburton, G. A. E. Vandenbosch, M. Ameloot, V. V. Moshchalkov, and T. Verbiest, "The role of chiral local field enhancements below the resolution limit of second harmonic generation microscopy," *Opt. Exp.*, vol. 20, no. 1, pp. 256–264, Jan. 2012.